

Strain hardening and heterogeneous deformation during twinning in Hadfield steel

C. Efstathiou^{a,*}, H. Sehitoglu^{b,*}

^a *Cornell University, Mechanical and Aerospace Engineering, 188 Rhodes Hall, Ithaca, NY 14853, USA*

^b *University of Illinois, Department of Mechanical Science and Engineering, 1206 W. Green St., Urbana, IL 61801, USA*

Received 21 July 2009; received in revised form 21 October 2009; accepted 28 October 2009

Available online 5 December 2009

Abstract

We identify the role of deformation twinning and twin–twin intersections on the strain hardening behavior of Hadfield steel single crystals using strain field measurements. In situ and ex situ strain field measurements resolved at micrometer length scales are obtained using digital image correlation. Ex situ measurements reveal that macroscopic twin-bands, which are composed of a mixture of fine twin-lamella and matrix material, generate approximately 30% axial strain. This measurement is comparable to strain predictions based on twinning crystallography. In situ measurements reveal that primary and secondary twins may nucleate simultaneously, but the primary twin-system remains predominantly active with increased deformation. The intersection of primary and secondary twin-systems was directly linked to an increase in the strain hardening response.

© 2009 Acta Materialia Inc. Published by Elsevier Ltd. All rights reserved.

Keywords: Manganese steel; Secondary twinning; Digital image correlation (DIC); Low stacking fault energy; Fcc alloy

1. Introduction

Hadfield steel is an austenitic manganese steel that possesses high wear resistance, high toughness and high strain hardening rate in polycrystalline form. These properties have made it successful in industrial applications that include impact hammers, crusher jaws, grinding mill liners, crawler treads for tractors, and railroad crossings. The high strain hardening rate of Hadfield steel is one of its most important properties, and it has warranted many investigations over the past 40 years [1–14]. The deformation mechanisms responsible for the high strain hardening rate include interactions between interstitial carbon atoms and dislocations [1,6], interactions between dislocations and twins [2–5,7,8], and interactions between twinning systems [14]. In polycrystals, it is difficult to experimentally isolate

the contribution of each deformation mechanism because generally all three are active, and because of grain boundary effects [1–3,6]. To circumvent these complexities, experiments are typically conducted on single crystals. In addition to utilizing single crystals, in situ optical investigations have proven valuable for identifying the dominant deformation mechanisms [5,8]. From these previous investigations and others, twinning is established as the primary deformation mechanism at the onset, and at early stages of deformation for tensile loading of $\langle 111 \rangle$ oriented Hadfield steel single crystals [5,7,8,14]. We focus on these crystals to provide a more detailed description of the deformation evolution (both spatially and temporally).

Optical observations indicate that twins form in a localized manner in Hadfield steel [5] single crystals. To date, however, no local strain field measurements have been made to directly link particular deformation features in the microstructure to the strain hardening behavior of Hadfield steel. Since the strain hardening behavior is the rate of change of the stress with respect to strain, it is most appropriately studied in situ. To fulfill these experimental requirements, we

* Corresponding authors. Tel.: +1 516 884 5778 (C. Efstathiou), tel.: +1 217 333 4112; fax: +1 217 244 6534 (H. Sehitoglu).

E-mail addresses: chris@neteamsolutions.com (C. Efstathiou), huseyin@illinois.edu (H. Sehitoglu).

utilize in situ digital image correlation (DIC). The purpose of the current study is to illustrate how particular twins and twin–twin intersections influence the strain hardening response by measuring the axial local strain fields.

Although no previous investigations have incorporated in situ strain field measurements, researchers have conducted in situ optical microscopy, and post-deformation electron microscopy studies. Early work on Cu single crystals showed that activation of primary twinning alone would reduce the work hardening rate, but when primary twins interacted with secondary twins, the hardening rate increased [15]. More recently, Chumlyakov et al. [14] and Karaman et al. [7] have noted that the strain hardening rate can be nearly 0 GPa when one twin-system is present, and can reach up to 7 GPa when multiple twin-systems are present in $\langle 111 \rangle$ oriented Hadfield steel single crystals.

The strain hardening contribution of twins has generally been considered from a macroscopic viewpoint as microstructural refinement similar to the Hall–Petch effect [8,16]. Similar to grain boundaries, twin-boundaries subdivide the microstructure and are obstacles to dislocation motion [16–18]. Dislocations in the matrix can interact with twins and result in glide that may not be favorably oriented with respect to the loading direction. In addition, few dislocation sources can operate in twins since they are very thin [8,18,19]. In Hadfield steel single crystals, twins appear optically as macroscopically uniform regions. However, these regions are in fact non-uniform, and contain a mixture of alternating regions of twin-lamella and matrix material often separated by 100–200 nm. Since twins form in a spatially heterogeneous manner, we utilize DIC to obtain strain field measurements at length scales between 13 and 145 μm . Although we do not resolve the axial strain within individual twin-lamella, we measure the axial strain generated by twin-bands and intersecting twin-bands which are a mixture of twin-lamella and matrix material. In this way we elucidate the contribution of deformation twinning to the macroscopic stress–strain behavior, and describe the degree of strain heterogeneity during deformation.

2. Background

Hadfield steel has a face-centered cubic (fcc) crystal structure and a low stacking fault energy (SFE) (23 mJ m^{-2}) [3]. The major alloying components in Hadfield steel are approximately 10–14 wt.% Mn and 1–1.4 wt.% C. In Hadfield steel, manganese lowers the SFE [20]. SFE describes the energy of the interface between a perfect (ABCABC) stacking sequence and a faulted (ABABAB) stacking sequence of a crystal. Stacking faults readily form in fcc crystals between Shockley partial dislocations because the energy associated with two partial dislocations is less than a perfect dislocation. The measure of SFE is important because it governs the distance between partial dislocations. This distance affects mechanisms such as cross-slip which allow dislocations to bypass obstacles. The formation of stacking faults are pre-

cursors to twin formation as previously noted in Refs. [21,22].

The mobility of dislocations also dictates the deformation mode (i.e. slip or twinning), which inevitably alters the macroscopic mechanical behavior, and material properties such as yield strength, creep resistance, age hardening and strain hardening behavior. At the atomic level, slip and twinning are shear-dominated mechanisms that crystals exploit to accommodate deformation. Crystal planes sheared by slip are localized, whereas crystal planes sheared by twinning involve a homogeneous shear between crystal planes. Slip rotates the crystal lattice gradually, whereas twinning rotates the lattice abruptly. Both mechanisms leave the crystal structure and lattice parameters unaltered, but depending on the crystal structure, twinning may require a “shuffle” to accomplish this [23–25]. Although some aspects of twinning are distinctly different from slip as mentioned above, dislocation structures are often incorporated in theories of twin nucleation and growth.

Twin growth theories have been developed by Christian [26] and Cottrell and Bilby [27]. Christian proposed the propagation of twin faults by dislocation reflection at the crystal surface or grain boundaries. The theory proposed by Cottrell and Bilby is fundamentally different since it requires a dislocation to dissociate into partial dislocations. Venables modified this theory for fcc metals (called “the pole mechanism”) by assuming that the dislocation dissociates into a glissile Shockley and a sessile Frank partial [28]. The sessile partial is the anchored “pole” and the glissile twin-dislocation revolves about this “pole” dislocation. Each revolution of the twin-dislocation generates twinned material [29]. A more recent theory proposed by Mahajan and Chin [30] suggests that three-layer twins are the twin nucleus, and these are composed of sessile and glissile groups of dislocations. The twin nucleation theories briefly mentioned above involve motion of partial dislocations which are driven by shear stress.

Partial dislocations as well as perfect dislocations generally obey a resolved shear stress law, and therefore Schmid factors can be determined for slip and twinning. The Schmid factor for twinning is taken as the Schmid factor for the leading partial dislocation. Since the Schmid factor for the leading partial dislocation is different under uniaxial tension and compression, twinning in fcc crystals is asymmetric. That is, twinning in fcc materials occurs by shear on the $\{111\}$ plane in the $[11\bar{2}]$ direction but not in the $[\bar{1}\bar{1}2]$ direction [22]. This is distinctly different from the motion of perfect dislocations which can occur on a $\{111\}$ plane in either the $[\bar{1}10]$ or $[1\bar{1}0]$ direction. Table 1 shows the Schmid factors under tension and compression, and the number of active systems for slip and twinning. Note that three twinning systems have the same Schmid factor for $\langle 111 \rangle$ oriented crystals under tension. We also note that the $\langle 111 \rangle$ orientation is more conducive to twinning in tension (0.31) compared to compression (0.16).

Competition between slip and twinning is dependent on the resolved shear stresses. The resolved shear stresses in

Table 1

Maximum Schmid factors for slip, twinning, and the leading and trailing Shockley partial dislocations. The number of systems which have equivalent Schmid factors is represented by the superscript. These values were taken from Ref. [7].

	Tensile				Compressive			
	Slip	Twin	Trail	Lead	Slip	Twin	Trail	Lead
(111)	0.28 ⁶	0.31 ³	0.16	0.31	0.28 ⁶	0.16 ⁶	0.31	0.16
(001)	0.41 ⁸	0.23 ⁸	0.47	0.23	0.41 ⁸	0.47 ⁴	0.23	0.47
(123)	0.46 ¹	0.47 ¹	0.34	0.47	0.46 ¹	0.34 ¹	0.47	0.34

single crystals are a function of the crystal orientation and the applied stress-state. Since the crystal orientation may be altered during deformation, the resolved shear stresses are influenced by the degree of deformation. This is referred to as geometric hardening, and in fcc materials, for example, this is a result of a slip plane and direction rotating toward the tensile axis during deformation. This effect becomes significant at strains greater than approximately 10% during slip deformation, whereas it is immediately significant for twinning. Note that the rotation of the slip direction differs for slip and twinning since the slip directions differ for a perfect and partial dislocation when considering one active system. Additionally, the extent of deformation may introduce multiple slip and multiple twinning in certain orientations as is implied by the number of active systems in Table 1. This can lead to an unusual strain hardening response with complicated interactions of deformation mechanisms and complex microstructural evolution [7,8].

3. Materials and methods

Hadfield steel single crystals with a composition of Fe–12.3Mn–1.3C (wt.%) were grown using the Bridgman technique in a helium atmosphere. The single crystals were subjected to a homogenizing treatment at 1100 °C for 24 h in inert gas atmosphere. Specimens were electrodischarged machined to a dog-bone shape with nominal dimensions of $10 \times 3 \times 1.5 \text{ mm}^3$ in the gage section. Specimens were then solution treated at 1100 °C for 1 h, and water quenched.

Uniaxial tensile testing was conducted at room temperature on a servohydraulic load frame. Specimens were loaded in position control which resulted in macroscopic strain rates of the order of 10^{-4} .

In situ macroscopic imaging was used to investigate the deformation evolution. Images of the specimen surface were captured with an IMI model IMB-202FT CCD camera ($1600 \times 1200 \text{ pixels}^2$). A Navitar optical lens was used for in situ observations, which generated a resolution of $2.5 \mu\text{m pixel}^{-1}$. DIC was performed on images obtained in situ to determine the evolution of the local strain field during deformation. In addition to in situ DIC, ex situ DIC was performed on images obtained after deformation using an Olympus optical microscope. The ex situ DIC measurements were used to establish the axial twinning strain magnitude. For these measurements, an optical mag-

nification of $25\times$ was used, which generated a resolution of $174 \text{ nm pixel}^{-1}$.

We utilized a two-dimensional DIC technique to measure the axial and the transverse in-plane displacement components. Two-dimensional tensorial strain field calculations were made from measurements of the in-plane displacement components. All strain fields presented in this paper are the spatial distribution of the axial strain component of the two-dimensional strain tensor.

The DIC technique measures displacement fields by tracking a random speckle pattern on the specimen surface [31]. Speckle patterns were applied to the surface of polished specimens using an Iwata Micron B airbrush. To perform DIC, a region of interest is selected in the reference image and is then divided into small square regions called subsets. In order to find the location of a deformed subset and its shape change, optimization techniques are employed in which values of displacement and linear displacement gradients of a subset are obtained. The resulting displacement field is then differentiated to obtain the strain field according to a central difference scheme.

Usually, the first image (before any applied load) is chosen as the reference image, and all others are compared against this one. Thus each correlation, and each strain field, represents the total strain. This is how the local strain fields were produced for studying the evolution of deformation twinning, and the axial twin strain magnitude.

On the other hand, to study the evolution of the strain hardening rate, a slightly different approach was used. Since the strain hardening rate is the rate of change of stress with respect to strain, an incremental approach was taken. To identify the “currently” deforming regions in the strain field, and to link these features to the hardening behavior, we segmented the nominal stress–strain curve into three regions. The first and the last image of each segment are correlated. By using this approach, the actively deforming regions during each deformation segment are illustrated, and thus particular deformation features can be linked to the change in macroscopic stress.

Commercially available software (Vic2d) from Correlated Solutions was used to perform the image correlation and the strain field calculations. The average macroscopic or “nominal” strains are calculated as the mean of the entire strain field. Further details on the application of DIC can be found in Ref. [31] and a general background on DIC is given in Ref. [32].

Table 2
Maximum theoretical axial twinning strains calculated using Eq. (1).

	Tensile (%)
$\langle 111 \rangle$	37
$\langle 001 \rangle$	41
$\langle 123 \rangle$	41

To characterize twinning using DIC, the measured local strain fields will be compared to the theoretical axial twinning strain as well as the trace of the angle of the twinning plane. The theoretical axial twinning strain is shown in Table 2, and is calculated using the following equation [29]:

$$\epsilon = \sqrt{1 + 2S \sin(\chi) \cos(\lambda) + S^2 \sin^2(\chi)} \quad (1)$$

where the twinning shear strain, $S = 0.707$ for the fcc crystals considered, and χ and λ are the angles between the loading direction and the twin-plane and the shear direction, respectively.

Fig. 1 shows an optical micrograph of a primary twin-band that is inclined approximately 54° to the loading axis. The twin-band is composed of alternating layers of fine twin-lamella and matrix material. The width of each twin-lamella is estimated to be less than $1 \mu\text{m}$. Since a fraction of the twin-band is matrix material, it is expected that experimental measurements made on a mesoscale inherently contain an average of the twin strain and the matrix strain. Furthermore, theoretical predictions of the axial twin strain at the mesoscale must also be based on a “rule-of-mixtures” calculation to facilitate a comparison with experimental measurements.

The primary twin-band in Fig. 1 is called a first-order twin; four possible first-order twin orientations exist for twinning from the original crystal lattice. We refer to the most frequently observed orientation as the “primary” twin, and other orientations are “secondary” twins. Often, primary twins intersect secondary twins, and the inter-

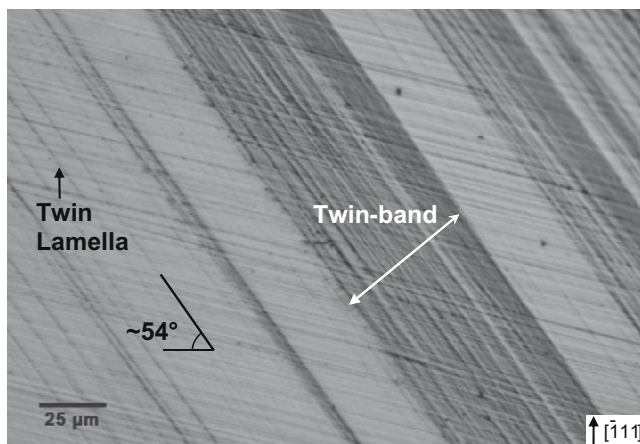


Fig. 1. An optical micrograph showing that twin-bands are composed of alternating layers of fine twin lamellae (black) and matrix material (white). Note that the inclination of the twins with respect to the tensile loading axis (vertical) is approximately 54° , which indicates they are from the primary twin system.

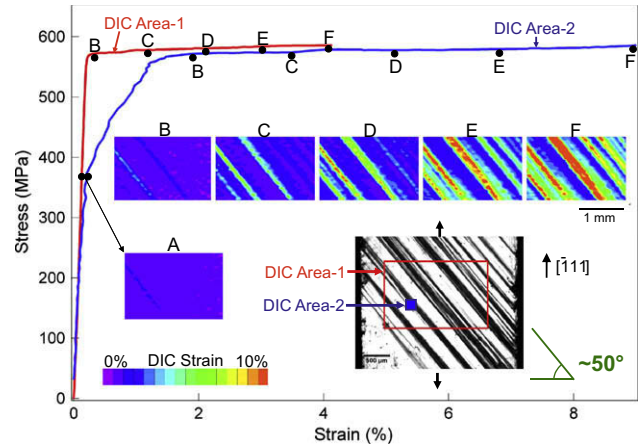


Fig. 2. The average axial stress–strain response for two areas of interest, and the strain fields calculated from DIC for corresponding points along the curve. A post-deformation optical micrograph indicates where the DIC analysis was conducted.

sected volume forms a twin within a twin. Mullner et al. have successfully modelled these twin–twin intersections using disclinations, and have described their contribution to strain hardening in austenitic steels [33,34].

Twins forming within first-order twinned regions are termed second-order twins. A total of 12 possible second-order twins orientations exist [35]. In other words, second-order twins are simply twins forming in already twinned region of a crystal. In fcc crystals the trace of the primary twin on the surface of a crystal makes an angle of approximately 70° to the second-order twin. Note the subtle difference between second-order twins and “secondary” twins. Secondary twins are first-order twins, and used in this paper to distinguish between the four possible first-order twin orientations.

4. Results

The results are divided into two sections which correspond to two different specimens. The first section will present the deformation behavior associated with primary twinning. The second section will reveal the deformation behavior associated with intersections of primary and secondary twins. In both sections, the strain field evolution and the average stress–strain response is shown for a particular specimen area. These areas are indicated on post-deformation optical micrographs to assist interpretation of the strain fields.

4.1. Primary twinning and axial twin strain evolution

As previously mentioned, twin formation in Hadfield steel typically occurs in localized regions of the specimen. Fig. 2 shows the average axial stress–strain behavior for a large specimen region (red stress–strain curve, area 1),¹

¹ For interpretation of color in Fig. 2–4, 6 and 7, the reader is referred to the web version of this article.

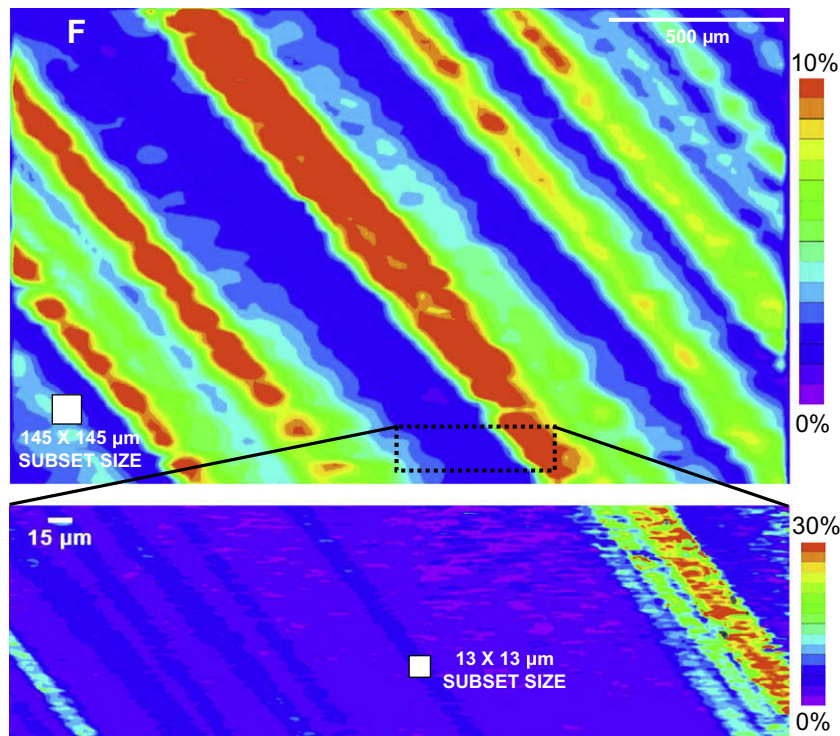


Fig. 3. Comparison of low-magnification and high-magnification axial strain fields for the region outlined by the black dashed box. Note that the higher-magnification results show numerous twin-bands with significantly higher strains. Each result has a different strain color scale bar. Recall that the low-magnification strain field (F) indicates the final state of the specimen after the loading shown in Fig. 2.

and for a smaller specimen region (blue curve, area 2). The corresponding areas are shown on the post-deformation micrograph of the specimen surface. The micrograph of the specimen surface shows alternating regions of matrix (white) and twin-band (black) material. Note that area 1 represents a region that appears to have approximately equal amounts of matrix and twin-band material, whereas area 2 represents a region that appears to encompass only one twin-band by the end of the loading. The twin-bands in this specimen are primary twins since they are inclined approximately 54° to the loading direction. The apparent twin nucleation stress, determined by the yield point in the stress–strain curve, is approximately 580 MPa for area 1, and 350 MPa for area 2. The average strain at the completion of the experiment is approximately 4% for area 1, and approximately 9% for area 2. These considerable differences in twin nucleation stress and axial twin strain are elaborated below with reference to the strain field measurements.

The strain fields labeled A–F were obtained in area 1 (this region includes area 2), and each strain field corresponds to an average strain indicated by a black circular marker on the stress–strain curve. At early stages of the deformation, shown by strain field A, a narrow blue region representing a twin-band appears faintly in the strain field. Since this twin-band constitutes only a small fraction of the area, the average stress–strain response does not deviate from linearity (red curve). In contrast, since the twin-band constitutes a large fraction of area 2, the average stress–

strain response deviates from linearity at approximately 350 MPa. As the nominal deformation increases (marker B), the stress–strain curve for area 1 indicates a yield point at approximately 580 MPa. It is apparent that consideration of the measurement length scale and location is important for the detection of the onset of twinning.

With increased deformation (markers C–F), additional twin-bands appear in the area, while others accumulate strain (shown by the green and red narrow bands). At the end of the loading, the maximum strain in any twin-band region is approximately 10%. The maximum strain is considerably smaller than that predicted by Eq. (1), and shown in Table 2 for loading along the $\langle 111 \rangle$ orientation. The smaller measured twin strain at this optical magnification is primarily a consequence of the measurement length scale. This effect is shown in the subsequent figure which compares the results obtained at low optical magnification with the results obtained at higher optical magnification.

Fig. 3 shows the strain field obtained at low magnification (from point F in Fig. 2), and at high magnification. The comparison is made in the region outlined by the dashed black box. In this region the low-magnification results appear to be “smoothed-out” compared to the high-magnification results. For example, in the left half of the dashed box, the low-magnification results show two fairly uniform regions (a blue region and a small green region), whereas the high-magnification results show seven separate twin-bands. In the right half of the outlined box, the high magnification results show a twin-band with

strains of up to 30%. Note that the high-magnification strain field indicates small strains (less than 1%) surrounding twinned regions, which suggests that nearly no macroscopic slip deformation accompanies the twin formation.

The measured strain within the twin-band of the high-magnification results in Fig. 3 is approximately 30%, but axial strain predictions based on twinning crystallography (see Table 2) suggest they should be as large as 37%. The smaller measured twin strain is a consequence of an incomplete twinned volume fraction within the twin-band region as opposed to strain-averaging effects. Thus, an estimate of the fraction of twinned material within the twin-band is made by dividing the measured strain by the theoretical strain ($\frac{30}{37} = 0.8$). This suggests approximately 80% of the twin-band is twinned material, and 20% is undeformed matrix material. The subset size is included in this figure to show that the twin-band is larger than the subset size, and therefore strain-averaging effects in the twin-band region from surrounding matrix material are minimized. This also supports the estimate that the twinned volume fraction is less than 100%. Although for this region the twin-band is larger than the subset size, other specimen areas have nucleated only individual twin-lamella, which are a small fraction of the subset size. In these regions, the maximum strains are influenced by strain averaging and this is why several of these twin-band regions (shown as blue bands) indicate only approximately 8% strain.

4.2. Twin–twin Intersections and strain hardening behavior

Fig. 4 shows the stress–strain curve and the local strain fields obtained for the specimen with intersecting twins. Note that the average stress–strain response shows significant strain hardening as compared to that shown in Fig. 2. A post-deformation optical micrograph is also shown in the figure for comparison. In this specimen, wide twin-bands form which are ultimately larger than the subset size, and so the maximum measured strains of approximately 30% within these regions approach theoretical strains. Close inspection of the strain fields show that the strain interfaces are not sharp, and significant strain (8%) has accumulated between the primary twin-bands, which is due to the formation of secondary twins.

To illustrate the microscopic details of the regions between the primary twin-bands, high-magnification post-deformation optical micrographs are shown in Fig. 5. Fig. 5a and b show intersecting twins, and Fig. 5c shows non-intersecting twins which exist but to a much lesser extent. The intersected region of two twins can form a second-order twin. A second-order twin is a twin that has formed within an already twinned region of a crystal as described in Ref. [35]. Although these micrographs are post-deformation, in situ DIC captured the strain fields associated with the interaction of these twins.

To identify how specific twin–twin intersections influence the overall strain hardening behavior, we conducted image correlation over segments of the entire loading his-

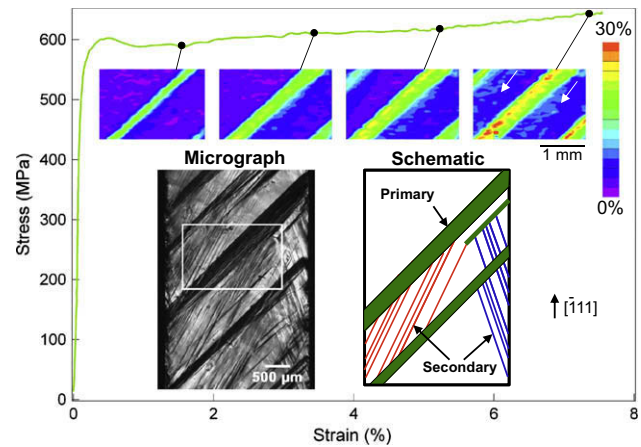
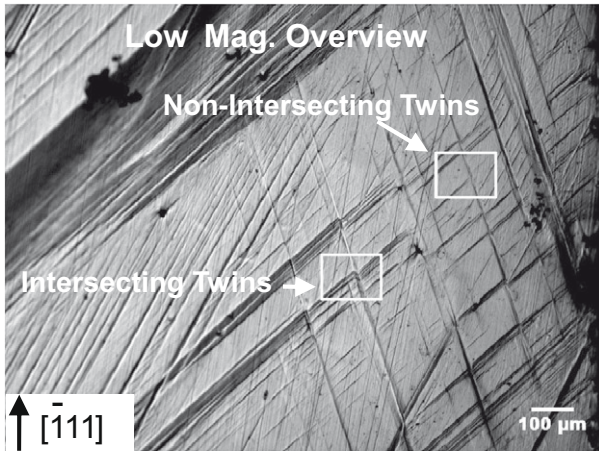


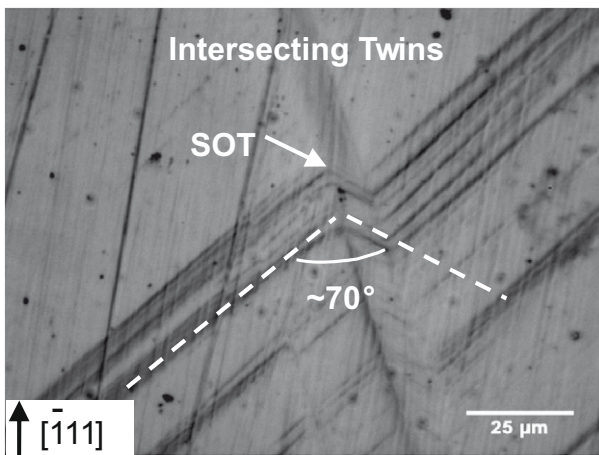
Fig. 4. The nominal stress–strain response, and the axial strain fields calculated from DIC at selected points along the curve. A post-deformation optical micrograph of the specimen surface with a white box indicates where the DIC strain fields are reported. Three twin-systems are identified, and for the purposes of clarity they are represented in the schematic as primary and secondary.

tory as explained in Section 3. By doing this we are able to identify the “currently” deforming regions and thus we can deduce the interactions which contribute to the strain hardening behavior. Furthermore, by using DIC we are able to consider the length scale effect on the upper and lower estimates of the strain hardening behavior.

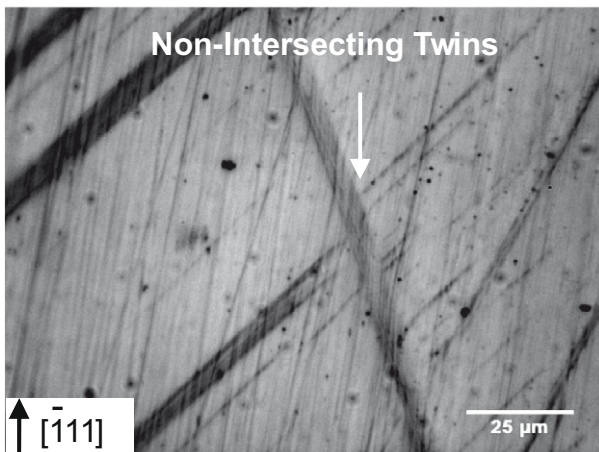
Fig. 6 shows the strain field corresponding to three segments of the loading history for the sample which displayed intersecting twins. The strain fields represent the total strain accumulated during each segment. The segments of the loading history are shown by the three corresponding horizontal arrows which represent approximately 1% average strain. Also shown is the hardening rate for the specimen which exhibited intersecting twins (blue curve) and for the specimen which did not exhibit twin–twin intersections (red curve). We emphasize again that by segmenting the loading history, the strain resulting from the intersecting twins during segment 1 does not contribute to the measured strain field in segment 2. The strain field during segment 1 indicated multiple twin-systems activated accompanied by a relatively high strain hardening rate (1.2 GPa). At a later stage of deformation shown by segment 2, the strain field indicated only one operative twin-system and a low strain hardening rate (0.3 GPa). In fact, the strain hardening rate reached a minimum value which was comparable to the sample which did not display intersecting twins (red curve). During segment 3, the strain field again indicated multiple operative twin-systems accompanied by a relatively high strain hardening rate (1.2 GPa). An important point to note is the region in the strain field identified by the white arrow. In this region, the strain field evolution shows that twin–twin intersections at early stages of deformation (segment 1) do not inhibit twin formation at later stages of deformation (segment 3). Furthermore, note that significant spatial heterogeneity is apparent during the evolution.



(a) 5x



(b) 50x



(c) 50x

Fig. 5. Optical micrographs showing the intersection of twin-bands after moderate applied deformation (less than 10% strain). (a) Low-magnification overview shows all three twin-systems (one primary and two secondary) have activated. Some regions show intersecting twins, whereas others show non-intersecting twins. (b) A high-magnification detail of a twin–twin intersection which has formed a second-order twin (SOT). (c) A high-magnification detail of a non-intersecting twin.

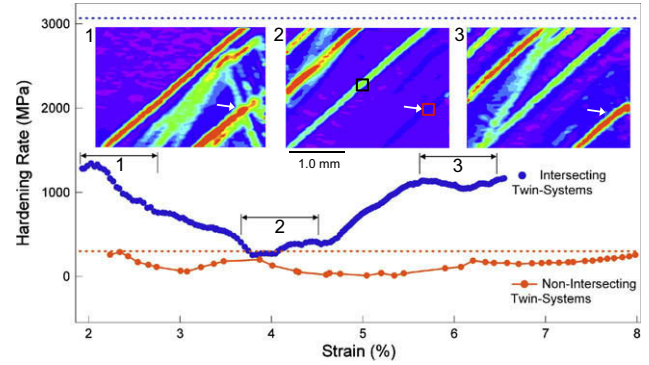


Fig. 6. Evolution of the strain hardening rate for increasing applied deformation for the specimen with twin intersections (blue curve), and without twin intersections (red curve). The three strain fields represent the accumulated deformation during each “segment” bracketed by the black arrows for the specimen which exhibited twin–twin intersections. The strain fields thus qualitatively compare periods of twin–twin intersection activity (segments 1 and 3), and a period with very little activity (segment 2). Note that the strain hardening rate is higher when twin–twin intersections are present. The dotted red line represents the maximum strain hardening rate found in a $200 \mu\text{m}^2$ region (red dotted box), and the dotted black line represents the minimum strain hardening value obtained in a $200 \mu\text{m}^2$ region at the center primary twin-band (black dotted box). The strain fields are scaled 0–5% to show the details. A white arrow points to a particular twin–twin intersection which is shown in Fig. 7

To show the extent of the spatial heterogeneity, two dashed lines have been included in Fig. 6. The dotted red line represents the maximum strain hardening rate of approximately 3 GPa in a $200 \times 200 \mu\text{m}^2$ sample region within the red box, and the dotted black line represents the minimum strain hardening value of approximately 0.3 GPa in a $200 \times 200 \mu\text{m}^2$ sample region within the black box. This shows that the strain hardening rate can differ spatially by up to an order of magnitude. It is expected that with increased applied deformation, the magnitude of the spatial heterogeneity could become larger since some actively deforming regions eventually become saturated and no strain further accumulates in these regions.

Post-deformation optical micrographs of the region with twin–twin intersections are shown in Fig. 7. The upper left micrograph in this figure shows a low-magnification overview of the twin–twin intersections, and a red box which encompasses the particular twin–twin intersection which was previously pointed out by the white arrow in Fig. 6. This particular region is encompassed by the red box, and it is shown at successively higher magnification to illustrate the secondary twin, and the second-order twins. The intersection involves an abrupt change of the orientation (approximately 70°) of the primary twin, which is consistent with theoretical predictions. Apparently, this twin–twin intersection did not completely inhibit growth of a primary twins since the evolution of the strain-field measurements

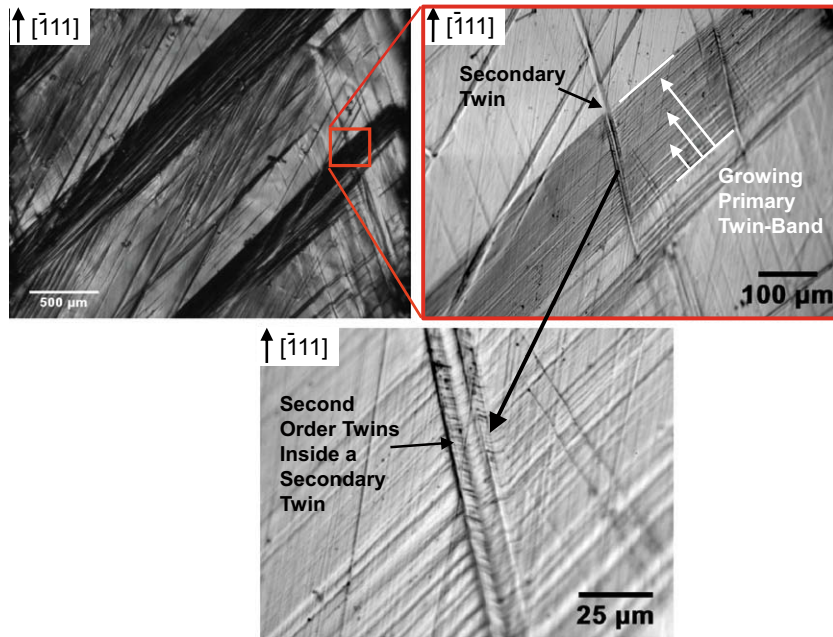


Fig. 7. Shows an overview of the specimen surface with a small red box outlining the twin–twin intersection, and increasingly higher-magnification images showing the second-order twins.

indicated accumulated strain within the primary twin-band at a later stage (segment 3 in Fig. 6).

5. Discussion

The strain field measurements show the evolution of the axial strain component during deformation twinning. A noticeable characteristic of deformation twinning in Hadfield steel is the formation of narrow bands with relatively large local strain. For example, the average strain within a twin-band can be approximately 30% whereas in the surrounding matrix regions the strain may be only 0.5% (see Fig. 3). This suggests that only small amounts of slip deformation in the surrounding matrix material accompany the formation of twins at initial stages of deformation. Since twinning dominates from early stages of plastic deformation, it is reasonable to conclude that the twinned volume fraction increases linearly with deformation only at early stages of deformation. At later stages of deformation, multiple twin-systems become more active, and the degree of twin–twin intersections increases. Increased twin–twin intersections can lead to increased slip deformation, as well as twin dissolution from detwinning reactions [36]. With these additional operative mechanisms at later stages of deformation, the resulting twin volume fraction evolution may no longer increase linearly. A comparison of measured and theoretical axial twinning strain within twin-bands gives an estimate of the twinned fraction as approximately 80%. This is the maximum twinned fraction at mesoscopic (300 μm) length scales. Of course, if the measurement length scale is decreased to the length scale of an individual twin-lamella, the volume fraction approaches 100%. Con-

sidering area 1 in Fig. 2, an estimate of the twinned fraction is 21% at 4% nominal strain.² Previously published model predictions for macroscopic specimen regions indicate approximately 21% twinned fraction by approximately 6.5% macroscopic strain, which is in general agreement with the current experimental estimates [7].

The spatial distribution of twin-bands was dependent on the applied deformation. Twin-bands nucleate several hundred micrometers apart and accumulate strain according to the order in which they formed. This suggests that regions containing existing twins act as nucleation sites for subsequent twins. This has been described before as Luders-type twin propagation [5]. Although the majority of the twin nucleation occurs near twin-bands, individual twin-lamellae are observed within the microstructure. These individual twin-lamellae have probably formed at stress-concentrations from microstructural heterogeneities. Apparently these isolated individual twin-lamellae are not as effective nucleation sites as larger twin-band regions; however, these twin-lamella regions are expected to grow at later stages of deformation.

The strain field measurements are particularly useful in understanding heterogeneous deformations which would be difficult to explain using conventional extensometer measurements. For example, consider the single twin-band which was nucleated at the onset of the yielding behavior at a significantly lower macroscopic stress (350 MPa) in

² This is estimated by mapping the strains to equivalent twin fractions similar to the prediction of the maximum twinned fraction estimates. Mapping strains to equivalent twinned fractions is a first approximation since slip deformation is considered to be very small.

Fig. 2. This particular twin-band must have nucleated from a stress concentration along the edge of the sample surface. We speculate this because the stress level increased to 580 MPa and remained constant with further deformation while under position control. It is obvious that if an extensometer was used to determine the twin nucleation stress it would be highly dependent on its placement along the specimen gauge length, and dependent on which surface it was attached to.

The utility of DIC is further exemplified in the analysis of twin–twin intersections. An outstanding result of the strain field measurements was that the presence of a secondary twin does not eliminate growth of the primary twin-band; however, it provides additional resistance to twin nucleation. The twin–twin intersections generated a definite increase the strain hardening rate from 0.2 to 1.2 GPa. Karaman et al. [8] reported a value of approximately 1.75 GPa for a specimen with 20% applied plastic strain. Note that just like the estimate of twin-fraction, the estimate of the strain hardening rate depends on the measurement length scale. It was shown that at particular regions with significant amounts of twin–twin intersections, with average local strains near 20%, hardening rates as high as 3 GPa were measured.

The formation of second-order twins in twin–twin intersected regions does not appear to eliminate growth of the primary twin-band. However, they do appear to increase the strain hardening rate. Second-order twin formations in austenitic steels were modelled by Mullner et al. [33] using disclinations. They showed that second-order twins are energetically favorable, and that the second-order twins increased the work hardening rate. This is consistent with what we observe. Interestingly, they also suggest that second-order twins require the presence of stress or strain concentrations. Since we observed the simultaneous nucleation of multiple twin-systems at relatively small applied deformations, which is not typical, we speculate that stress concentrations in the microstructure or at the specimen edges could have promoted the nucleation of multiple twin-systems and hence the twin–twin intersections. It is expected that with increased deformation, twin–twin intersections and second-order twin generation would increase, and dislocation–twin interactions would additionally contribute to the strain hardening rate.

6. Summary and concluding remarks

In situ strain field measurements were shown to be particularly useful for describing the evolution of twin-band formation, and twin–twin intersections. Using strain field measurements at high optical magnification, a quantitative measure of the axial twinning strain was obtained. A maximum twinning strain of approximately 30% was measured in some twin-band regions. These measurements were comparable to theoretical predictions for the twinning of a $\langle 111 \rangle$ oriented Hadfield steel single crystal under tension.

The comparison of measurements to theoretical predictions suggested that 80% of the twin-band region was twinned.

We conclude that twin–twin intersections do not completely inhibit growth of the primary twin-system; however, a definite increase in the strain hardening response is attributed to the intersections. Additionally, the measurement length scale was shown to influence the strain magnitude, and thus estimates of strain hardening rate can spatially vary by up to an order of magnitude.

Acknowledgements

We thank the reviewer for useful comments on the manuscript. The work was supported by the National Science Foundation Division of Materials Research DMR-0803270 and partially by the National Science Foundation Division of Civil, Mechanical and Manufacturing Innovation CMMI-0926813.

References

- [1] Raghavan AS, Sastri KS, Marcinkowski MJ. Nature of work-hardening behavior in Hadfield's manganese steel. *Trans Metall Soc AIME* 1969;245:1569–75.
- [2] Dastur YN, Leslie WC. Mechanism of work hardening in Hadfield manganese steel. *Metall Trans* 1981;12A:749–59.
- [3] Adler PH, Olson GB, Owen WS. Strain hardening of Hadfield manganese steel. *Metall Trans* 1986;17A:1725–37.
- [4] Shtremel MA, Kovalenko IA. On the work hardening mechanism of Hadfield steel. *Phys Metals Metall* 1987;63:158–66.
- [5] Karaman I, Sehitoglu H, Gall KA, Chumlyakov YI. On the deformation mechanisms in single crystal Hadfield manganese steels. *Scripta Mater* 1998;38:1009–15.
- [6] Owen W, Grujicic M. Strain aging of austenitic Hadfield manganese steel. *Acta Mater* 1998;47(1):111–26.
- [7] Karaman I, Sehitoglu H, Gall KA, Chumlyakov YI, Maier HJ. Deformation of single crystal Hadfield steel by twinning and slip. *Acta Mater* 2000;48:1345–59.
- [8] Karaman I, Sehitoglu H, Beaudoin AJ, Chumlyakov YI, Maier HJ, Tome CN. Modelling the deformation behavior of Hadfield steel single and polycrystals due to twinning and slip. *Acta Mater* 2000;48:2031–47.
- [9] Karaman I, Sehitoglu H, Chumlyakov Y, Maier H, Kirkeva I. Extrinsic stacking faults and twinning in Hadfield manganese steel single crystals. *Scripta Mater* 2001;44(2):337–43.
- [10] Canadinc D, Sehitoglu H, Maier H, Chumlyakov Y. Strain hardening behavior of aluminum alloyed Hadfield steel single crystals. *Acta Mater* 2005;53(6):1831–42.
- [11] Chumlyakov YI, Kireeva IV, Zaharova EG, Luzginova NV, Sehitoglu H, Karaman IK. Strain hardening and fracture of austenitic steel single crystals with high concentration of interstitial atoms. *Russ Phys J* 2002;45:274–84.
- [12] Zaharova EG, Kireeva IV, Chumlyakov YI, Efimenko SP, Sehitoglu H, Karaman IK. Deformation mechanisms and strain hardening of Hadfield-steel single crystals alloyed with aluminum. *Doklady Phys* 2002;47:515–7.
- [13] Canadinc D, Karaman I, Sehitoglu H, Chumlyakov YI, Maier HJ. The role of nitrogen on the deformation response of Hadfield steel single crystals. *Metall Mater Trans* 2003;34A:1821–31.
- [14] Chumlyakov YI, Kireeva IV, Sehitoglu H, Litvinova EI, Zaharova EG, Luzginova NV. High-strength single crystals of austenitic stainless steels with nitrogen content: mechanisms of deformation and fracture. *Mater Sci Forum* 1999;318–320:395–400.

- [15] Mori T, Fujita H. Twinning deformation in single crystals of Cu-8 at.% Al alloy. *Trans Jpn Inst Met* 1977;18(1):17–24.
- [16] Remy L. Twin-slip interaction in fcc crystals. *Acta Metall* 1977;25(6):711–4.
- [17] Mahajan S, Chin G. The interaction of twins with existing substructure and twins in cobalt–iron alloys. *Acta Metall* 1974;22(9):1113–9.
- [18] Remy L. The interaction between slip and twinning systems and the influence of twinning on the mechanical behaviour of fcc metals and alloys. *Metall Trans A* 1981;12(3):387–408.
- [19] Venables JA. *Deformation twinning*. New York: Gordon and Breach Science Publishers; 1964.
- [20] Schramm RE, Reed RP. Stacking fault energies of seven commercially austenitic stainless steels. *Metall Trans* 1975;6:1345–51.
- [21] Hirth J, Lothe J. *Theory of dislocations*. 2nd ed. Malabar, FL: Krieger Publ. Co.; 1992.
- [22] Kibey S, Liu J, Johnson D, Sehitoglu H. Energy pathways and directionality in deformation twinning. *Appl Phys Lett* 2007;91(18):181916-1-3.
- [23] Barrett CS. *Cold working of metals*. Cleveland: American Society of Metals; 1949.
- [24] Cahn RW. Plastic deformation of alpha-uranium; twinning and slip. *Acta Metall* 1953;1:49–52.
- [25] Rosenbaum HS. *Deformation twinning*. London: Gordon and Breach Science Publishers; 1964.
- [26] Christian JW. Theory of transformation in pure cobalt. *Proc Roy Soc A* 1951;206:51–64.
- [27] Cottrell AH, Bilby BA. A mechanism for the growth of deformation twins in crystals. *Phil Mag* 1951;42:573–81.
- [28] Venables JA. Deformation twinning in face-centered cubic metals. *Phil Mag* 1961;6:379–96.
- [29] Hall EO. *Twinning and diffusionless transformations in metals*. London: Butterworth Scientific Publications; 1954.
- [30] Mahajan S, Chin G. Formation of deformation twins in f.c.c. crystals. *Acta Metall* 1973;21(10):1353–63.
- [31] Chu T, Ranson WF, Sutton MA, Peters WH. Applications of digital-image-correlation techniques to experimental mechanics. *Exp Mech* 1985;25:232–44.
- [32] Dally JW, Riley WF. *Experimental stress analysis*. 4th ed. Knoxville: College House Enterprises, LLC; 2005.
- [33] Mullner P, Solenthaler C, Speidel M. Second order twinning in austenitic steel. *Acta Metall Mater* 1994;42(5):1727–32.
- [34] Mullner P. Between microscopic and mesoscopic descriptions of twin–twin interaction. *Z. f. Metallkunde* 2006;97:205–16.
- [35] Dunn CG. Standards for identifying complex twin relationships in cubic crystals. *Trans Am Inst Mining Metall Eng* 1945;161:90–7.
- [36] Li A, Chumlyakov Y, Korotaev A. Influence of the fine structure of twins on strain hardening as a result of repeated twinning. *Fizika Metallov i Metallovedenie* 1988;65(4):809–15.